

# Analysis of Gas Turbine Combustor Exhaust Emissions: Effects of Transient Inlet Air Pressure

Oscar Tenango-Pirín, Sierra Espinosa,\* Juan Carlos García, and José Alfredo Rodríguez

Gas turbine combustors are often subjected to combustion instabilities because of variability of operating conditions, affecting components, and altering exhaust emissions. Herein, the analysis focuses on simulating numerically the non-premixed combustion as unsteady flamelet combustion and detailed kinetic mechanism. The goal is analyzing exhaust gases under unsteady inlet airflow conditions to define operation guidelines. The numerical approach is validated using data from the literature for nonperturbed cases. Three periodical perturbations of different amplitude show differences with the nonperturbed case. Besides emission of exhaust gases, the temperature field is sensitive to airflow inlet conditions. According to the simulation results, a strong dependence of temperature and pressure in primary and dilution zones of combustor exists on the inlet air pressure condition. Emissions of flue gases like CO and NO<sub>x</sub> respond to combustor thermal behavior showing high sensitivity to inlet air pressure as well. Results indicate that moderate pressure oscillations may derive into flashback effects.


## 1. Introduction

Gas-fueled turbines design and operation continues to attract the attention due to technoeconomic reasons. Environmentally, goals like reducing emissions and noise have forced to design more quiet and efficient combustion systems. However, the interaction of air and fuel may happen under off-design conditions and may develop alterations on the exhaust products. These conditions may be a function of time, like transient fluctuations of inlet streams, not considered in original design, such as the case of pressure fluctuations of air coming from the compressor. One reason may be faults of compressor operation, for instance, due to fouling by stick dust particles, which has been reported, highlighting that roughness of blades due to fouling may alter the compressor performance by reducing the flow rate.<sup>[1,2]</sup> Furthermore, the increments of combustion chamber inlet temperature and turbine exhaust temperature due to compressor fouling are the focus of attention.<sup>[3]</sup> The fact that combustor inlet

air may fluctuate due to compressor operating malfunction, and it may affect the structure of the engine, requires a deep understanding. One strategy consists in analyzing the compressed air fluctuations and tries to simulate the phenomenon numerically, revising first the complexity, because the characteristics of temperature field and flame dynamics are a function of several factors. We can mention, for instance, the inlet swirl, the inlet momentum ratio, and the combustor geometry. Some works have tried to clarify the influence of flow conditions on gas turbine performance, but more questions arose. For example, changes of flow structure in oscillating premixed turbulent swirling flames showed there is an influence of modulated mass flows on the flame dynamics and temperature field;<sup>[4]</sup> also, found that both swirl strength and amplitude fluctuations

of burning velocity influenced on local form of fluctuating temperature. Laminar flame speed of certain fuels like biomass syngas also influences flow recirculation, flame shape, and temperature fields in premixed swirl burners.<sup>[5]</sup> Other effects of swirling levels leading to highly rotating vortex are nozzle turbine blades damage due to changes in chamber exit flow.<sup>[6]</sup> Rotating vortex also plays a main role on species formation. They have the capacity to modify residence times and, in turn, have an influence on the formation of some intermediate species, such as CO. Lee et al.<sup>[7]</sup> and Habib et al.<sup>[8]</sup> found that combustion primary air swirler angle has an effect not only on rotating flow but also on NO<sub>x</sub> production. Hence, flow conditions define not only the increase of internal energy rate but also the formation of some pollutant gases. Flames behavior undergoing to combustion instabilities deserved the attention too.<sup>[9]</sup> Flame sheet dynamics under acoustically forced flames was the target analyzing a range of perturbation frequencies and amplitudes. The results showed shear layer instabilities that deform the flame through acoustic forcing rendering flame growth and decay for downstream distance. In addition, the flame front propagated at constant speed with no dependence on downstream position or perturbation amplitude. On the other hand, thermal radiation modeling remains active because radiation defines temperature conditions on flame and liner walls of the combustor.<sup>[10]</sup> In summary, combustion instabilities due amplifying/attenuating the acoustics or for a wide range of frequencies are still misunderstood.<sup>[11,12]</sup> Likely flames are sensitive to combustion instability and to oscillations of low frequency.<sup>[13]</sup> Therefore, in planning this investigation authors assumed that pressure fluctuations

O. Tenango-Pirín  
Universidad Autónoma de Ciudad Juárez  
Av. Plutarco Elías Calles 1210, Ciudad Juárez, Chihuahua 32310, México  
S. Espinosa, J. C. García, J. A. Rodríguez  
Universidad Autónoma del Estado de Morelos  
Av. Universidad 1001, UAEM, Cuernavaca, Morelos 62209, México  
E-mail: fse@uaem.mx

 The ORCID identification number(s) for the author(s) of this article can be found under <https://doi.org/10.1002/ente.202301093>.

DOI: 10.1002/ente.202301093

alter flow dynamics and local increase of internal energy leading to combustion instabilities. Studies of potential risks derived from combustion instabilities include Toffolo et al.,<sup>[14]</sup> which presented a computational fluid dynamics (CFD) analysis of self-sustained thermoacoustic oscillations generated by changes in internal energy and acoustic modes in the combustor. They found that heat released fluctuated at frequencies close to the natural frequency of the chamber. Sohn and Cho<sup>[15]</sup> found that under these conditions, strong oscillations of pressure can emerge, and those oscillations can lead to the premature failure of turbine components, as reported by the authors.<sup>[16,17]</sup> Recent studies tried to optimize the operating characteristics of turbine combustor. Predicted turbine inlet fuel and air temperature, fuel mass flow, nozzle fuel distribution, operating pressure of combustor,  $\text{NO}_x$ , and temperature of combustor inlet air responded to artificial neural network input parameters like turbine exhaust temperature and design parameters.<sup>[18]</sup> However, little attention on predicting inlet air pressure temporal fluctuation and consequent transient exhaust emissions still represents a drawback for gas turbine combustor operation. For instance, fluctuations of inlet air pressure affect the combustion by increasing the flame temperature and specific heat of burned gases.<sup>[19]</sup> Although some investigations oriented the efforts to develop strategies for pressure instabilities control and mitigation,<sup>[20,21]</sup> a deep understanding of the effects of pressure variations on combustion processes may help to improve the design and operation of can combustors, as a recent review has revealed.<sup>[22]</sup> Gas turbines operators frequently report the failure of internal elements like blades, which affects its performance and efficiency.<sup>[2,3,23]</sup> There are several causes for blade failure like fatigue, oxidation, corrosion, and surface degradation among other, and many are related to the temperature and contents of combustion products, gases that leave the combustor. That is why an understanding of the possible causes of temperature rise and unsteady fluctuations in the combustor, as well as the generated products, can explain the status in the first stage of the turbine. For this reason authors conducted similar studies, but not using fully detailed kinetic models.<sup>[16,17]</sup> Thus, this work details modeling of time-dependent combustion to investigate pressure fluctuations and combustion process. A 3D CFD simulation resolves transient conditions and the possible effects of streams on combustor components. Modeling chemical kinetics used GriMech 3.0. Results from  $k-\epsilon$  turbulence model in predicting complex fluid behavior inside the can combustor are discussed. The validation of the numerical approach stands on comparing the present results for velocity and temperature in the combustor against measured data found in the literature for a similar combustor operated under normal conditions.<sup>[24]</sup> Transient peaks of temperature due to pressure imbalances change accordingly. Further, effects of pressure affected CO and  $\text{NO}_x$  production, which may aid in design and operation of the combustion chamber.

## 2. Operational Conditions and Geometry

The combustion chamber under study thermally feeds a 70 MW gas turbine in a combined cycle power plant. They are in coaxial arrangement with the compressor and turbine, but not aligned.

The geometry with primary and secondary air precedes dilution air zones shown in **Figure 1a**, which includes dimensions from datasheet in mm, not to scale. In this figure, labels  $P_1$ – $P_7$  correspond to stations for several monitors positioned on chamber axis to obtain transient behavior information of pressure and temperature. The group of 15 can combustors interconnect to each other through two crossfire pipes; one is part of **Figure 1b**. Crossfire pipes location coincides with primary air zone, which feeds the burner, on  $P_2$ .

Interior burner appears in **Figure 1b**, which contains surrounding holes for cooling air streams. Meanwhile, the flame tube configuration includes air dilution entrance by six holes of 23 mm diameter. Primary air streams enter through six holes of 38 mm diameter, allowing burn out any fuel residues to ensure complete combustion.<sup>[17]</sup> As observed in **Figure 1b**, the burner works in swirl mode using two concentric pipes for mixing gas–fuel and air. The fuel injector is central hole supported by eight peripheral holes of 5 mm diameter. These holes are oriented an angle of  $45^\circ$  with respect to the axial direction to promote tangential motion of the evacuated flow, making complex the fluid patterns, as shown elsewhere.<sup>[16,17]</sup> The swirler is outer diameter 241 mm, and has 20 channels distributed every  $18^\circ$  from each other to let inlet air pass through. This air inlet generates recirculation downstream the fuel injector for enhancing the air–fuel mixing.

Boundary conditions in **Table 1** represent can combustor operation conditions.<sup>[16]</sup>

Most boundary conditions of the model were defined as inlets, outlets, and walls (see **Figure 1a** and **Table 1**). The mainstream inlets of the domain were defined according to **Table 1**. A turbulence intensity of 10% and hydraulic diameter for each inlet were defined as turbulence parameters. At outlet, the operating pressure condition was assigned. The no-slip condition was applied for velocity at walls in all coordinate directions. Physical properties of gases such as density and heat capacity were calculated with the probability density function (PDF) approach and mixing law, respectively, while the thermal conductivity was considered constant. Also, due to the type of cells used, a second-order discretization scheme was used for momentum and energy equations. Residuals of convergence criterion were assigned to  $1 \times 10^{-6}$  for energy and  $1 \times 10^{-5}$  for the remaining variables reaching the convergence in all calculated cases.

Parameters like angular frequency and mass flow rate defined as in operator data sheets and the turbine's operation guide, while measured data for pressure and temperature provided by power plant personnel. All boundary conditions served to conduct numerical simulations assuming nonadiabatic condition, while combustion of fuel species assumes to react under lean mixture with oxidant. The species considered in the combustion are shown in **Table 2**, for natural gas as fuel composed by methane/ethane blend where methane is 90 vol% being oxidizer hot air at 650 K from compressor exit.

## 3. Strategy of Simulation

Mesh independence for can combustor warrants accuracy of predicted results as follows.

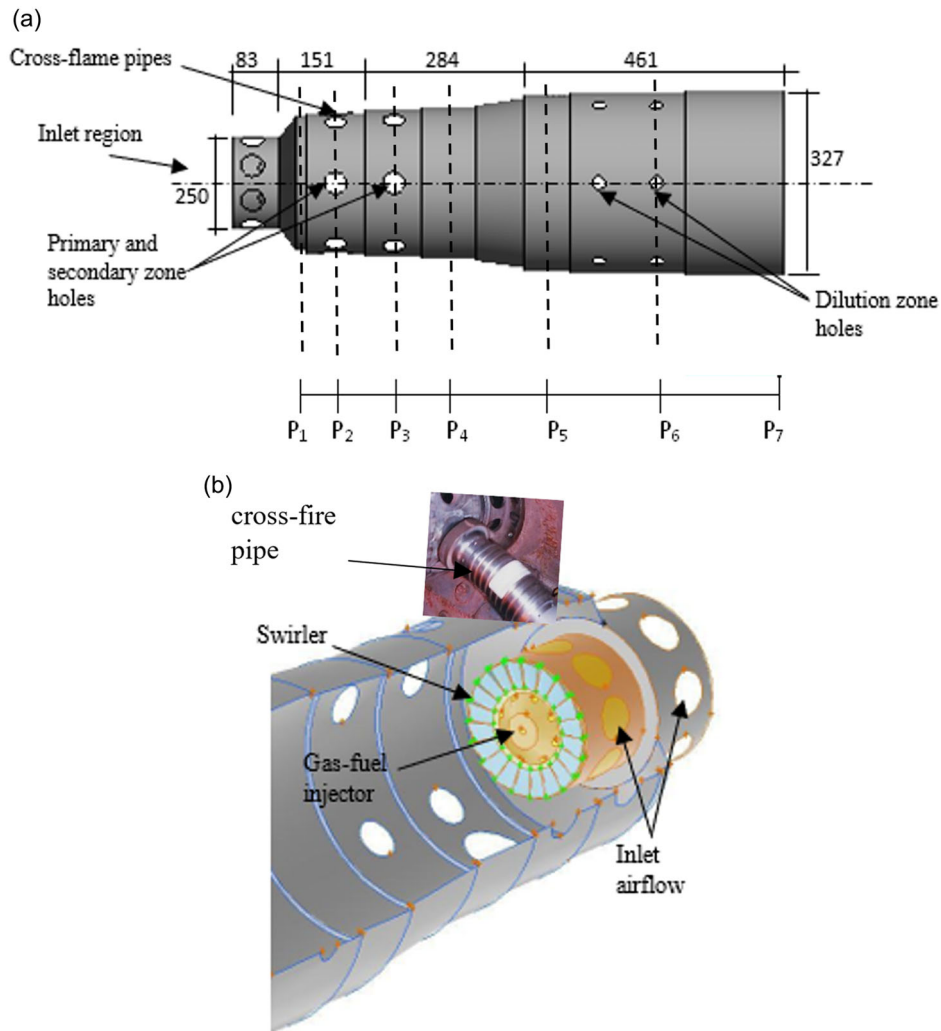


**Figure 1.** Geometry of can combustor; a) main flow stream inlets including cross-flame pipes; b) combustor interior: burner and swirler; outer: cross-fire pipe interconnects with a sister chamber.

**Table 1.** Boundary conditions defined according to registered data.

Variable	Magnitude	Comments
Pressure of gas in gas injector, $P_{gas}$	$1.46 \times 10^6$ Pa	Constant/pressure inlet
Pressure amplitude of airflow at inlet, $P_{airin}$	A = 6, 9, 12 kPa	Set of simulations, Equation (19)
Pressure at primary zone holes	839.3 kPa	Constant/pressure inlet
Pressure at dilution holes	839.1 kPa	Constant/pressure inlet
Angular frequency, $\omega$	8.5 Hz	Constant
Average temperature of vane wheel	842.4 K	Measured on last stage of turbine rotor/wall
Temperature of the can combustor shell	750 K	Measured on compressor discharge as cooling air condition/wall
Total air mass flow rate	$13.3 \text{ kg s}^{-1}$	Composition is shown in Table 2
Total fuel mass flow rate	$0.23 \text{ kg s}^{-1}$	Composition is shown in Table 2
Cross-flame pipes	–	Periodic zone
Grills air inlets	839.1 kPa	Constant/pressure inlet
Combustor outlet	817.5 kPa	Constant/pressure outlet

**Table 2.** Natural gas and species composition considered in combustion.

Species	Molecular weight
CO <sub>2</sub>	44
CO	28
H <sub>2</sub>	2
H <sub>2</sub> O	18
O <sub>2</sub>	32
Species of fuel gas phase	Specific fraction (taken as mol%)
CH <sub>4</sub>	0.9197
C <sub>2</sub> H <sub>6</sub>	0.0803
Species of oxidizer	Molecular weight
O <sub>2</sub>	32
N <sub>2</sub>	28
Stabilization of flame	Temperature, K
Fuel	300
Air	650

### 3.1. Mesh Characteristics

The mesh is in **Figure 2a** showing type of cell, while a detail of the swirler shown in **Figure 2b** illustrates most of complexity of the geometry.

It is worth noting that position for each primary inlet air hole and cross-flame pipe is not radially equidistant, thus simulation assumed no symmetry. Therefore, this is a 3D computational domain built and solved with commercial program Fluent.<sup>[25]</sup> The complexity of geometry components in can combustor and demanding vortex fluid motion adapt to tetrahedral cells mesh. Mesh convergence analysis served to evaluate the mesh performance, through a grid convergence index (GCI). Equation (1)–(3) follow Roache<sup>[26]</sup> to calculate GCI, using a tangential component of velocity as testing variable due to swirl flow as follows:

$$GCI = \frac{3|e|}{r^s - 1} \quad (1)$$

$$e = \frac{u_2 - u_1}{u_1} \quad (2)$$

$$e = \frac{h_2}{h_1} \quad (3)$$

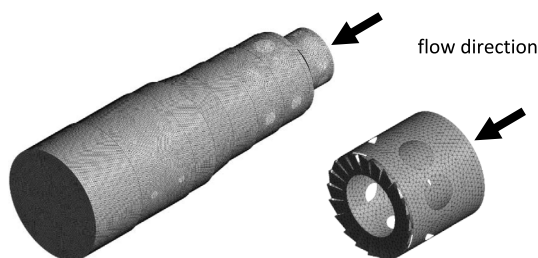


**Figure 2.** External view of the mesh: a) shell combustor with flame tube; b) swirler detail.

**Table 3.** Mesh convergence study.

Mesh	Number of cells	Cell size [mm]	Averaged tangential velocity [m s <sup>-1</sup> ]	GCI
1	913 337	1.5	1.72	
2	931 064	1.3	1.75	6
3	1 355 341	0.9	1.79	2.4
4	1 701 565	0.8	1.81	1.3
5	1 952 761	0.8	1.81	0.5

where  $e$  is the absolute error,  $r$  is the ratio of element size between fine and coarse meshes,  $s$  is the order of discretization scheme, second, and  $u_1$  and  $u_2$  are velocity values for fine and coarse meshes, respectively. The element sizes are  $h_2$  and  $h_1$ . Results for GCI for all tested computational meshes are in **Table 3**. The best GCI, 0.5, obtained for mesh 5 of  $1.95 \times 10^6$  cells, considered suitable for the present calculations is in the last row.

### 3.2. Turbulence Modelling

Equation (4)–(6) represent a time dependent solution of conservation of mass, momentum, and energy:

$$\frac{\partial \rho}{\partial t} + \nabla \cdot (\rho \vec{v}) = S_m \quad (4)$$

$$\frac{\partial}{\partial t} (\rho \vec{v}) + \nabla \cdot (\rho \vec{v} \vec{v}) = -\nabla p + \nabla \cdot (\hat{\tau}) + \rho \vec{g} + \vec{F} \quad (5)$$

$$\frac{\partial}{\partial t} (\rho E) + \nabla \cdot (\vec{v}(\rho E + p)) = \nabla \cdot \left( k_{\text{eff}} \nabla T - \sum_j h_j \vec{J}_j + (\hat{\tau}_{\text{eff}} \cdot \vec{v}) \right) + S_h \quad (6)$$

where  $\rho$  is the density,  $\vec{v}$  is the velocity vector,  $p$  is the static pressure,  $\hat{\tau}$  is the viscous stress tensor,  $\rho \vec{g}$  is the gravitational body force, and  $\vec{F}$  stands for external body forces.  $S_m$  is any user-defined source.  $E$  is the energy defined as a function of enthalpy,  $k_{\text{eff}}$  is the effective conductivity,  $h_j$  is the enthalpy of formation of species  $j$ , and  $\vec{J}_j$  is the diffusion flux of species  $j$ . The first three terms of the right side of energy equation represent energy transferred by conduction, species diffusion, and viscous dissipation, respectively. Finally,  $S_h$  considers volumetric heat of chemical reactions. Here, the source of energy  $S_h$  is:

$$S_h = - \sum_j \frac{h_j^0}{M_j} R_j \quad (7)$$

where  $h_j^0$  stands for enthalpy of formation of species  $j$ , and  $R_j$  is the volumetric rate of creation of species  $j$ .

The SIMPLE scheme was used for coupling of pressure and velocity. Reynolds-averaged Navier–Stokes equations,<sup>[25,27,28]</sup> RANS, consider turbulence effects<sup>[29,30]</sup> by solving the Reynolds stress tensor:

$$\dot{\tau} = \mu \left[ (\nabla \vec{v} + \nabla \vec{v}^T) - \frac{2}{3} \nabla \cdot \vec{v} I \right] \quad (8)$$

where the term  $\mu$  is the turbulent viscosity and  $I$  is the unit tensor. In Equation (8), the Boussinesq hypothesis is invoked,<sup>[25,29]</sup> which was solved by a two-equation  $k$ - $\epsilon$  model. The reader is referred to the specialized literature<sup>[29,30]</sup> for a deep understanding of RANS approach. The  $k$ - $\epsilon$  model uses two additional transport equations for the turbulent kinetic energy  $k$  and its viscous dissipation rate  $\epsilon$  represented by Equation (9) and (10) as follows:

$$\rho \frac{Dk}{Dt} = \frac{\partial}{\partial x_i} \left( \left( \mu + \frac{\mu_t}{\sigma_k} \right) \frac{\partial k}{\partial x_i} \right) + G_k + G_b - \rho \epsilon - Y_M \quad (9)$$

$$\rho \frac{D\epsilon}{Dt} = \frac{\partial}{\partial x_i} \left( \left( \mu + \frac{\mu_t}{\sigma_\epsilon} \right) \frac{\partial \epsilon}{\partial x_i} \right) + G_{1\epsilon} \frac{\epsilon}{k} (G_k + C_{3\epsilon} G_b) - C_{2\epsilon} \rho \frac{\epsilon^2}{k} \quad (10)$$

where  $G_k$  is the generation of turbulent kinetic energy due to mean velocity gradients and  $G_b$  is the generation of turbulent kinetic energy due to buoyancy.  $Y_M$  represents the contribution of the fluctuating dilatation in compressible turbulence to the overall dissipation rate. Finally,  $C_{1\epsilon} = 1.44$ ,  $C_{2\epsilon} = 1.92$ , and  $C_{3\epsilon}$  are constants, and  $\sigma_k = 1$   $\gamma_{\sigma_\epsilon} = 1.3$  are the turbulent Prandtl numbers, respectively.

### 3.3. Combustion Simulation

A combustion approach like non-premixed combustion model (NPCM) and the unsteady diffusion flamelet model were adopted.<sup>[25,31]</sup> The NPCM is a transported PDF model based on mixture fraction  $f$ , which represent the local mass fraction of burn or unburn elements of fuel in all the species. PDF-based models allow to predict temperatures and species in upstream locations of non-premixed flames with even better accuracy than eddy dissipation concept (EDC) model.<sup>[32]</sup> The NPCM model includes a transport equation to calculate position of the flame, considering an average mixture fraction  $f$  as

$$f = \frac{Z_i - Z_{i,ox}}{Z_{i,fuel} - Z_{i,ox}} \quad (11)$$

where  $Z_i$  is the mass fraction of species  $i$  and subscripts ox and fuel denotes oxidizer and fuel, respectively. Additionally, the continuity Equation (4) was solved in terms of the Favre mean mixture fraction averaged by density,  $\bar{f}$ , taking the form of Equation (12) as follows:

$$\frac{\partial}{\partial t} (\rho \bar{f}) + \nabla \cdot (\rho \vec{v} \bar{f}) = \nabla \cdot \left( \frac{\mu_t}{\sigma_f} \nabla \bar{f} \right) + S_{us} \quad (12)$$

where  $\mu_t$  is the turbulent viscosity and a constant  $\sigma_f = 0.85$  and  $S_{us}$  represents a source term described by a user-defined function, which is described later. Further to Equation (12), another conservation equation for the mixture fraction variance  $\bar{f}'^2$  was solved as

$$\frac{\partial}{\partial t} (\rho \bar{f}'^2) + \nabla \cdot (\rho \vec{v} \bar{f}'^2) = \nabla \cdot \left( \frac{\mu_t}{\sigma_t} \nabla \bar{f}'^2 \right) + C_g \mu_t (\nabla \bar{f})^2 - C_d \rho \frac{\epsilon}{k} \bar{f}'^2 + S_{us} \quad (13)$$

where  $f' = f - \bar{f}$ .  $C_g$  and  $C_d$  are constants with values of 2.86 and 2.0, respectively.

On the other hand, chemistry modeling for unsteady diffusion flamelet demands a converged solution for steady flamelet modeling as initial guess. Other successful works account for gaseous non-premixed combustion in can-type combustor.<sup>[33]</sup> Hence, a strategy of simulation for unsteady flamelet model allowed to predict both fast and slow-forming species, such as  $NO_x$ , with detailed chemical nonequilibrium due to straining effect of turbulence. Unsteady flamelet species calculation used Equation (14):

$$\rho \frac{\partial Y_i}{\partial t} = \frac{1}{2} \rho X \frac{\partial^2 Y_i}{\partial f^2} + S_i \quad (14)$$

where  $Y_i$ ,  $X$ , and  $S_i$  are the species mass fractions, the scalar dissipation, and the species reaction rate for the species  $i$ , respectively. Following, accurate flamelet generation uses chemical mechanism GriMech 3.0.<sup>[34]</sup> This mechanism includes thermodynamic data for 53 chemical species and 325 reactions.

A transport equation for probability marker applies for each flamelet located in space, from a steady-state converged flow. The transport equation for the marker probability is given by

$$\frac{\partial (\rho l_n)}{\partial t} + \nabla \cdot (\rho \vec{v} l_n) = \nabla \cdot \left( \left( \frac{k}{C_p} + \frac{\mu_t}{\sigma_t} \right) \nabla l_n \right) \quad (15)$$

where  $l_n$  is the  $n$ th flamelet,  $k$  is the laminar thermal conductivity of the mixture,  $C_p$  is the mixture specific heat, and  $\sigma_t$  is the Prandtl number.

On the other hand, heat losses by radiation follow a sphere model applied to the surface of the flame.<sup>[35]</sup> In this way, any changes in enthalpy which affect the final flame temperature are considered. In addition, given the operation conditions for fuel and temperature, a thermal- $NO_x$ -model applied for  $NO_x$  prediction. These gases are highly dependent on temperature level beyond 1800 K.  $NO_x$  formation follows Zeldovich mechanism for regimes of rich combustion<sup>[36]</sup> described by the reversible Equation (16)–(18):



### 3.4. Inlet Air Pressure Variation

The simulations considered two stages: one stage of stationary solutions served to compare the numerical approach with data from the literature; then, a second group of transient solutions included pressure perturbations at inlet. For first stage, Equation (4)–(6) stated the steady state of flow and combustion. For second stage, time-dependent solutions employed the set of

equation as they are. This last employed primary airflow pressure perturbations using Equation (19), to simulate a periodic inlet air pressure, expressed by time function  $P_{airin}$  to represent the unsteadiness of combustion:<sup>[16]</sup>

$$P_{airin}(t) = A \sin(\omega t) + P_m \quad (19)$$

where  $A$  is the amplitude,  $\omega$  is the angular frequency,  $t$  is the time step of integration, and  $P_m$  is the measured operating pressure. Magnitudes of  $A$  and  $\omega$  are given in Table 1. Note that amplitude  $A$  varied for second stage of simulations, as shown in Table 1, to investigate its influence on combustion process.

## 4. Results and Discussion

### 4.1. Validation of Numerical Approach

Steady-state solutions adapted to meet available data from another can combustor, served to validate the modelling approach, although differences with Goebel et al.<sup>[24]</sup> model still persisted due to geometry and operating conditions. For instance, present configuration had to be modified to mitigate air entrance downstream the inlet section. This condition was necessary to reach high swirl conditions detected in measured data of velocity.<sup>[25]</sup> Results for temperature, axial velocity, and swirl velocity normalized with the centerline values of temperature  $T_0$  and axial velocity  $U_0$ , and plotted against nondimensional radial distance  $r/R$ , respectively, served to make the comparison. Results shown in **Figure 3a** for normalized temperature indicate discrepancy between present CFD results and the reported experimental data, close to centerline, which reduces near the shell wall.

Both profiles show a peak around  $r/R$  of  $\pm 0.4$ , far from central region of the combustor. Similar results for both velocity profiles obtained in this region are in Figure 3b,c. The trend of experimental data and results obtained numerically is the same, with discrepancies found as the wall approximates. The differences are attributed to two reasons. The first one is due to the presence of a gap in fuel nozzle as part of experimental rig. This gap allowed additional air to enter, influencing the flow pattern and temperature field. The effect of this extra air stream supply can be interpreted as increase of axial velocity near the flame tube. Instead, the swirl velocity reduced, as can be observed in Figure 3c, leading to underprediction. This is because a gap in fuel nozzle was not considered in the numerical simulation. Meanwhile, the discrepancies in temperature are attributed to numerically assuming chemical equilibrium, while combustion was purely driven by mixing level and turbulence. Effect of assumption are underestimation of exothermic and endothermic reactions in regions near the wall, which are driven by chemical kinetics. Further, this happens but in lesser degree, in regions close to centerline. Despite discrepancies attributed to configuration differences of combustor, and given the similarities found in results for region near centerline of can combustor, the numerical predictions are consistently acceptable in reproducing the experimental data.

Additionally, the predicted flow field<sup>[37]</sup> compares well to measured data from the literature for one section around the burner, framed by dotted lines in the velocity vector field obtained by

particle image velocimetry (PIV), as shown in Figure 3e. The predicted axial velocity component, for oxygen concentration  $\beta = 0.21$ , limited by white lines describe two shear layers, on the PIV flow field as shown in Figure 3e. A shear layer region

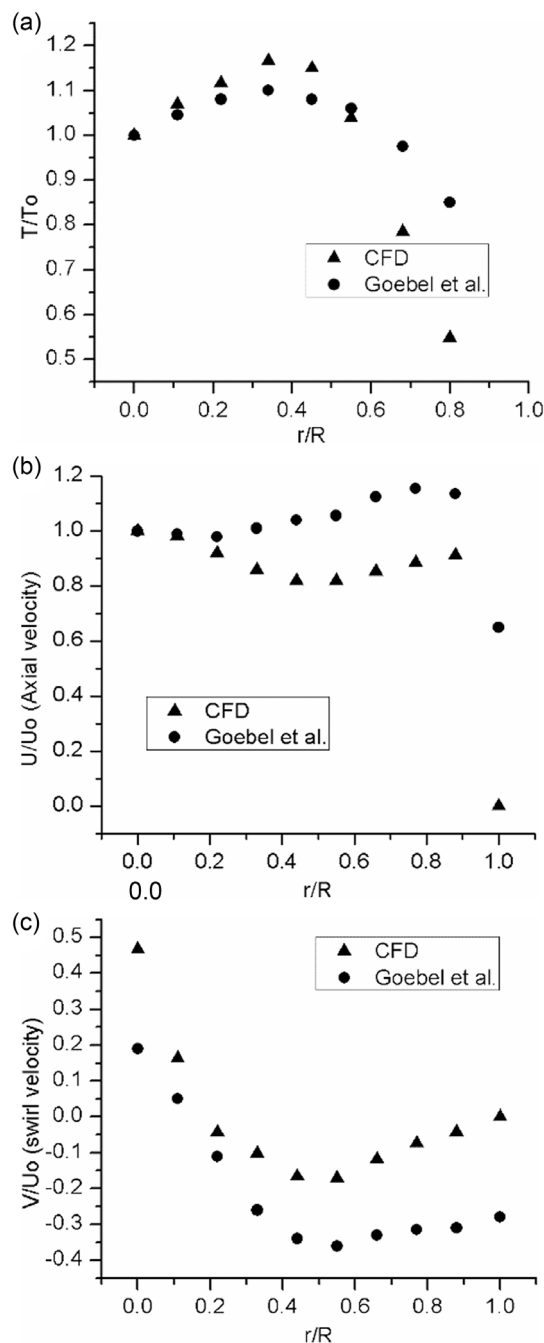


**Figure 3.** Validation of numerical approach using experimental data for combustor outlet: a) comparison of normalized profiles of temperature as a function of position against data from Goebel et al.;<sup>[24]</sup> b) *ibid.*, axial velocity; c) *ibid.*, swirl velocity; d) Production of CO as a function of equivalence ratio and oxygen concentration and comparison against data from Marsh et al.;<sup>[42]</sup> e) flow field as a function of oxygen concentration  $\beta = 0.21$  compared against PIV data from the literature.<sup>[37,42]</sup>



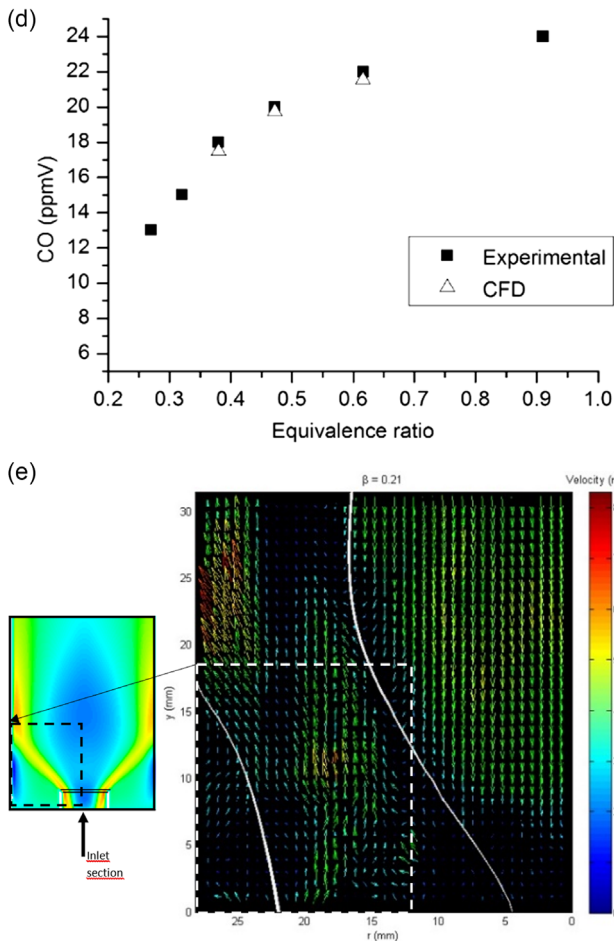


Figure 3. Continued.

of main flow, defined as zero axial velocity, is limited by recirculation cells. The limits for present predictions and experimental data are in good agreement, which constitutes a second validation of prediction approach. In general, the predicted results show good performance in reproducing the bulk flow in the can combustor, resolving the central zone of recirculation using a  $k-\epsilon$  turbulence model.<sup>[37]</sup> The validity of above comparison is emphasized with detailed calculation of absolute error between present predictions and data from the literature. This applies for each variable of Figure 3a–d, as observed in Table 4. For this purpose, the calculation of error was averaged by combustor zones. First zone is located at burner, in a region  $0 \leq r/R \leq 0.33$ ; a

Table 4. Comparison of results against data from the literature,<sup>[24]</sup> see Figure 3a–d.

Variable	$0 \leq r/R \leq 0.33$ % error	$0.34 \leq r/R \leq 0.66$ % error	$0.67 \leq r/R \leq 1$ % error
Temperature	1.94	6.27	18.98
Axial velocity	7.33	22.54	47.64
Swirl velocity	116.6	56.03	87.71
CO		2.2	

second zone is  $0.34 \leq r/R \leq 0.66$ ; and third zone falls near the shell wall of can,  $0.67 \leq r/R \leq 1$ . Table 4 shows in second column the error for temperature in central zone, where it is the lesser; in second zone the error grows and near the wall it is maximum nearly 20%. For axial velocity similar trend takes place, but error percentage increased due to the presence of the nozzle gap. Finally, for swirl velocity the error is very large in central zone due to experimental extra air entering through the gap. However, values shown for CO with dependence on equivalence ratio indicate averaged error of only 2.2%. This is observed in Figure 3d, where numerically tested equivalence ratios corresponding to zone  $0.34 \leq r/R \leq 0.66$  agree very well with experimental data in reproducing CO generation.

#### 4.2. Inlet Air Pressure Time Variation

Effects of imposed perturbations on inlet airflow pressure revealed other mixing and stream distributions in the combustor compared against the nonperturbed case. A time step of  $3.5 \times 10^{-4}$  s used follows Kim et al.<sup>[38]</sup> This integration time step allowed to describe in detail how pressure of inlet air changes with time, as shown in Figure 4. As will be shown, pressure plays a main role in temperature and flow structure within can combustor, in addition to products of combustion. This is due to the connection between thermal energy and momentum transport which are coupled by Equation (6). The amplitude of pressure in Figure 4 corresponds to 6 kPa, which varied to 9 and 12 kPa for subsequent investigation on effects.

#### 4.3. Effects on Combustor Temperature and Pressure Fields

Results for pressure and temperature, obtained by means of temporal monitors, describe their time-dependent behavior in can combustor. The monitors fixed in space were distributed along axial centerline of can combustor, starting on burner position  $P_1$  and subsequent locations to reach  $P_6$  (see Figure 1a), while  $P_7$  is reserved for exit condition. In analyzing any variable behavior as a function of time, the combustor length was divided in regions. Results for pressure in Figure 5a reveal that regions near burner,

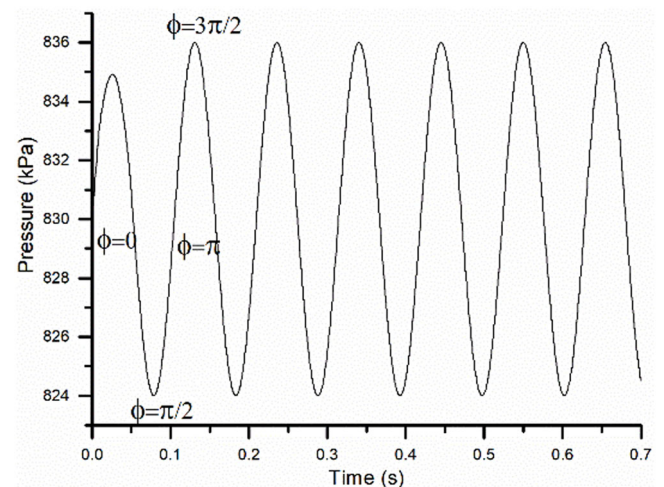
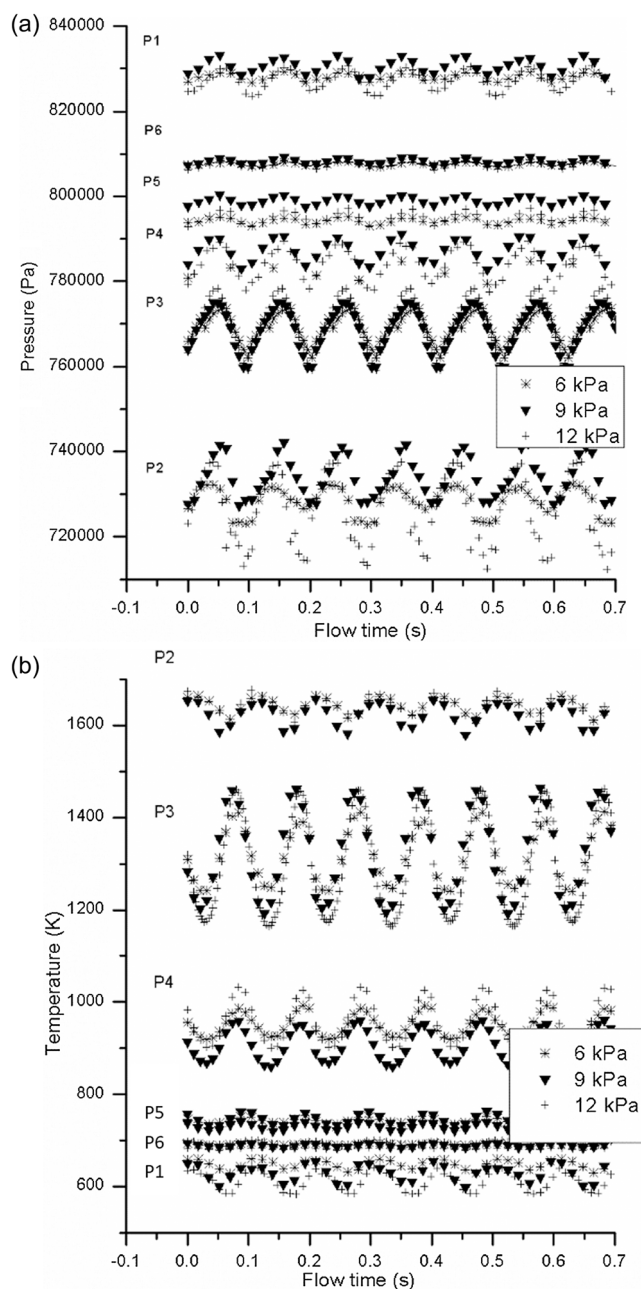


Figure 4. Periodic perturbation of pressure in inlet airflow.



**Figure 5.** Time-dependent normalized results in stations  $P_1$ – $P_7$  of can combustor: a) pressure behavior; b) temperature behavior.

primary air inlet, and secondary air inlet, profiles  $P_1$ ,  $P_2$ , and  $P_3$  are most influenced by pressure fluctuation than subsequent regions, such that region  $P_6$  is almost no longer influenced. This result indicates that highest flow instabilities were induced by interaction between different flows, making the mixing condition more complex and changing. Pressure values for  $P_1$  fluctuated due to the combination of perturbed primary air inlet, fuel inlet, and swirling effect. However, it should be noted that valleys for pressure exciting of 12 kPa go down even under corresponding operating pressure at 830 kPa. This indicates that gases invade regions up to the burner position, which was confirmed

through temperature contours, as shown ahead. Monitors for  $P_2$  revealed the most remarkable gaps of pressure for all inlet pressure variations.  $P_3$  and  $P_4$  also indicate large oscillation of pressure but reduced drastically for  $P_5$ . Further, monitor  $P_6$  placed at dilution zone was barely affected. In general, results for pressure indicate a stabilization of the flow from inlet to exit, as observed in  $P_1$ – $P_6$ . As observed in Figure 5a, pressure in all locations oscillates with same frequency as imposed inlet pressure perturbation. However, around the pipes for crossfire ( $P_2$  and  $P_3$ ) highest fluctuations of pressure occurs, likely making this a risk zone.

Similar results, but for temperature monitors, are in Figure 5b. It is remarkable that results for  $P_1$  are much lower temperature compared to  $P_2$ , which is due to condition of inlet region introducing primary air to start combustion, at time that fuel mixes with primary air flow. As observed, highest temperature values correspond to monitors  $P_2$  and  $P_3$ , where primary and secondary air streams induce consumption of most of fuel. About oscillation of temperature, the results reveal that it happens in  $P_3$ , while  $P_4$  shows considerable fluctuation to finally reduce in  $P_5$  and  $P_6$ . In general, temperature value and fluctuating amplitude reduce as exit region approximates. Furthermore, temperature oscillation also is in phase with inlet air pressure perturbation. One highlight aspect is that temperature level and amplitude resulted near the region around of crossfire pipes,  $P_2$  and  $P_3$ . This confirms the risk to which they are exposed, high pressure and temperature, likely related to previous reports of crossfire pipes damage.<sup>[16,17]</sup>

#### 4.4. Pressure Temporal Variation and Exhaust Gases Unsteadiness

Importance of emissions is linked to temperature, therefore worth analyzing the effects of inlet pressure increments from 6 to 9 kPa, and then to 12 kPa. Results as a function of time confirm it because exhaust gases were very sensitive to pressure of inlet air variation. Therefore, it can be said that species residence time and their diffusion respond to pressure. For simplicity, carbon dioxide, carbon monoxide, and  $\text{NO}_x$  are analyzed at combustor exit, on  $P_7$ , as shown in Figure 6a–c. By comparing transient trend of  $\text{CO}_2$  and CO against nonperturbed, shown in Figure 6a, higher concentration of  $\text{CO}_2$  corresponds to nonperturbed case, contrasting with low  $\text{CO}_2$  emission up to 30% lesser for pressure fluctuations. This result is interpreted as a reduced interaction between fuel and oxidant molecules as effect of pressure variation, driving to reduction of combustion efficiency. As consequence of  $\text{CO}_2$  emission, the remaining oxygen increases in flame zone. Besides  $\text{CO}_2$  emission reduction compared to unperturbed case, any increment of pressure perturbation causes  $\text{CO}_2$  amplitude to fluctuate, first reducing from 6 to 9 kPa and then increasing from 9 to 12 kPa. While pressure amplitude varies linearly,  $\text{CO}_2$  exhaust emission varies nonlinearly, highlighting the complexity of the process.

In contrast, Figure 6b shows that CO emission increases for any perturbed pressure. This is attributed to lesser oxygen molecules reacting with carbon to form  $\text{CO}_2$ , at time of producing more CO due to incomplete combustion. Further, for pressure increased, the amount of CO varied up to 0.7 ppm, although with



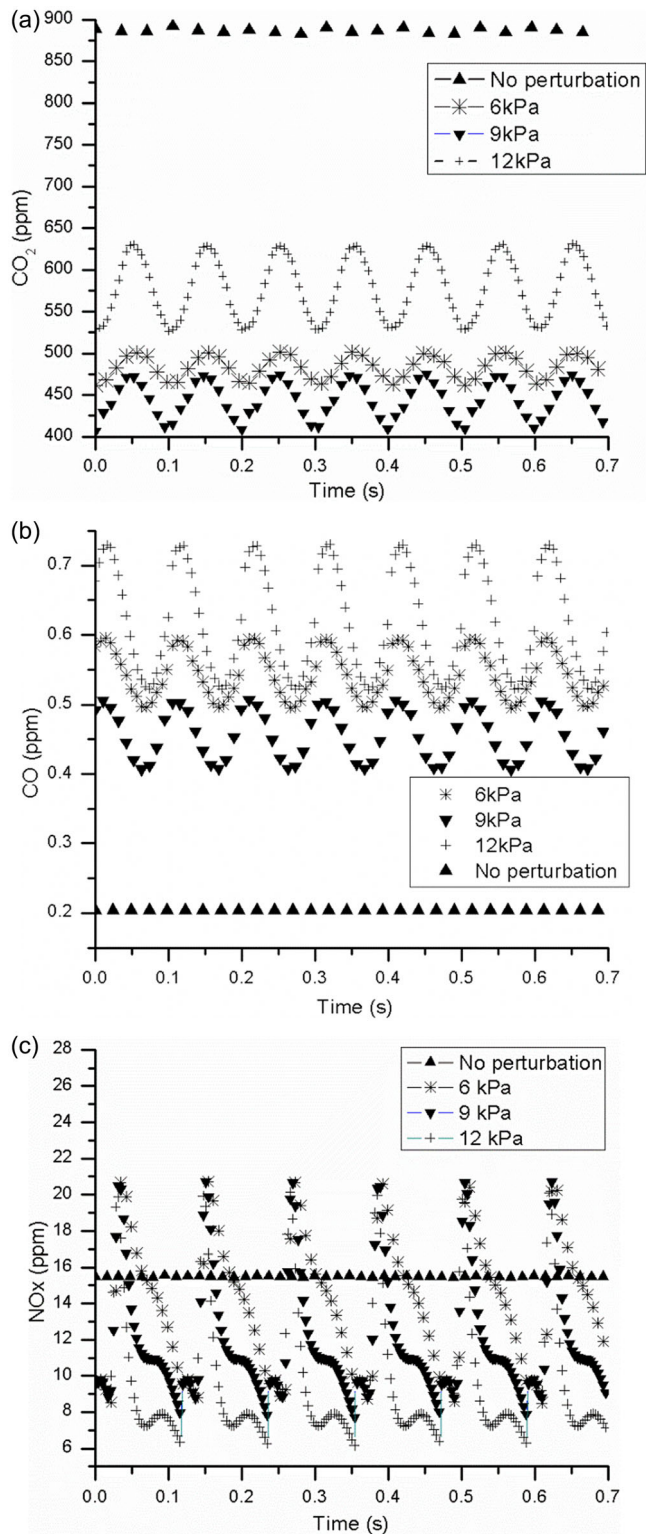


**Figure 6.** Effect of varying the amplitude of pressure perturbations on exhaust gases content at  $P_7$ : a)  $\text{CO}_2$ ; b)  $\text{CO}$ ; and c)  $\text{NO}_x$ .

marginal values in the range of  $\pm 0.2$  ppm, in contrast to the steady-state solution, with average of 2.6 ppm.

Regarding  $\text{NO}_x$  emission, timely values for each inlet pressure condition are in Figure 6c. It can be observed that  $\text{NO}_x$  frequency is different to air pressure at inlet. Oscillations of  $\text{NO}_x$  occur around the value obtained for nonperturbed case. However, some peaks of  $\text{NO}_x$  reach 21 ppm for all amplitudes of pressure perturbation tested, although valley of  $\text{NO}_x$  goes down to 6 ppm for highest amplitude of 12 kPa. This gas emission changes to 8 ppm for 6 and 9 kPa pressure perturbations. As production of  $\text{NO}_x$  was observed to be strongly attached to temperature inside the chamber, temperature was also evaluated at combustor outlet as follows.

#### 4.5. Temperature Field at Inlet and Outlet

Results shown in Figure 7 indicate that exit temperature was affected by unbalanced pressures. The nonperturbed solution shows slight fluctuations, while well-defined temperature oscillations respond to any perturbed pressure condition. As observed in Figure 7, temperature fluctuations reach up to 12, 15, and 25 K for pressure perturbations of 6, 9, and 12 kPa, respectively. In general, higher amplitudes of pressure perturbations conducted to higher temperature fluctuation. The frequency of fluctuation of temperature matched the frequency of pressure perturbation. This occurs to  $\text{CO}$  and  $\text{CO}_2$  but contrasting with  $\text{NO}_x$ . Among the critical risks of temperature fluctuations, it can be mentioned heating conditions are strongly linked to unstable thermoacoustic combustion. Combined heating and thermoacoustic conduce to useful life reductions of several elements, like a transition piece between combustor and turbine, known as the turbine nozzle and also like turbine blades, first stage.<sup>[16,39,40]</sup> Therefore, failure or fracture of turbine blades, first stage, due to thermal fatigue, is a function of transient stress, associated with transient phenomena like transient perturbations of pressure.<sup>[16,40,41]</sup>

As a result of pressure perturbation, it is observed that temperature field in can combustor may conduct to reverse flow. One region with this condition was observed for a pressure perturbation of 12 kPa amplitude, as shown in Figure 8a. Such a stagnation flow resulted in a region of high temperature located before

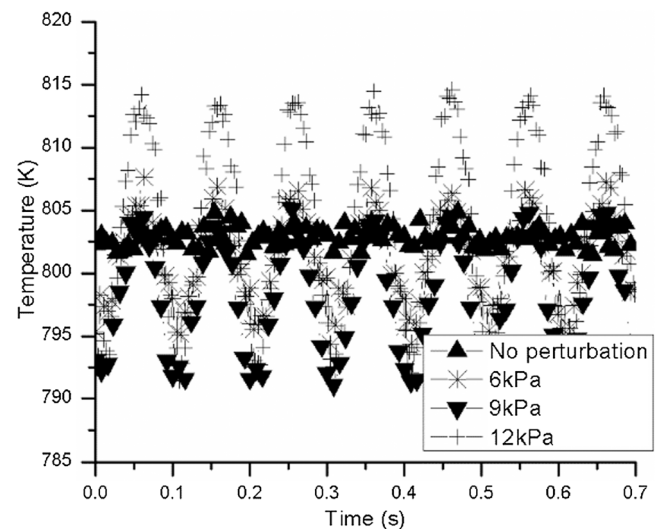


**Figure 7.** Effect of pressure perturbations on temperature at outlet.

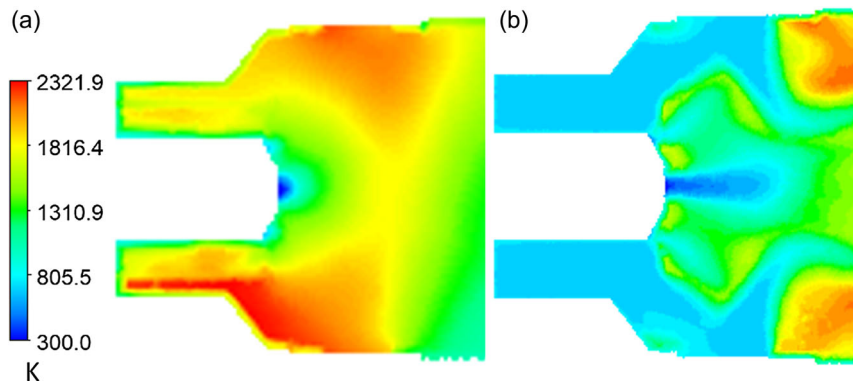


**Figure 8.** Contours of temperature in the inlet of inlet air: a) results for pressure increase, amplitude set to 12 kPa; b) results for pressure release condition.

the primary zone for times when air inlet pressure fluctuation increased, compared to the case of perturbed pressure reduction, as shown in Figure 8b. The effect was interpreted as a local pressure drop in the can combustor, characterized by negative velocities, which propagated the flame upstream the burner. This is known as flashback, taking place for combustion instability. Therefore, the risk that the flame reaches not only the inlet primary airflow but also the annular space between concentric pipes of burner increases drastically. Cyclic failure risk for some components is imminent, like fuel injector, which normally is not designed to resist flames of high temperature. It means that material is exposed to thermal fatigue or burning, as reported somewhere else.<sup>[41]</sup> When pressure releases, temperature reduces, as shown in Figure 8b. The pressure fluctuation defines both temperature and flow dynamics, with reverse flow as the main risk of failure in the inlet primary air region.

#### 4.6. Effects on Velocity and Turbulence Intensity

After strong pressure fluctuations were detected along the chamber, it was decided to analyze the velocity field. **Figure 9** and **10** show a comparison of flow characteristics between the nonperturbed stationary case and the case where a pressure fluctuation

of 12 kPa was imposed. For this, a time-dependent lowest pressure fluctuation was considered (see Equation (19)). Figure 9 displays a comparison of velocity distribution. For the stationary case, the flow patterns are well defined, and velocity distribution displays the formation of an oscillating vortex in the main flow. This is product of interaction with air inlets of secondary and dilution sections. In contrast, under pressure fluctuation there is different flow distribution and velocity was remarkably reduced causing the gases to reverse flow, in upstream direction. In this case, higher velocity fields take place at dilution section, which also caused a drop in temperature as observed above in monitors of Figure 5b.

On the other hand, the comparison in Figure 10 centers on turbulence intensity. The contours show highest turbulence for stationary case near outlet. This is due to interaction of combustion gases with air of dilution, coming from holes and grills. However, for the perturbed case, turbulence intensity increased drastically along combustor, due to oscillation on inlet pressure. A maximum turbulence percentage rounding 5 times higher for most turbulent zone was located at burner section. This is attributed to intense mixing of gases, generated by the pressure fluctuation combined with several streams in the primary zone. Results also revealed that gases are expelled from the chamber with high level of turbulence.

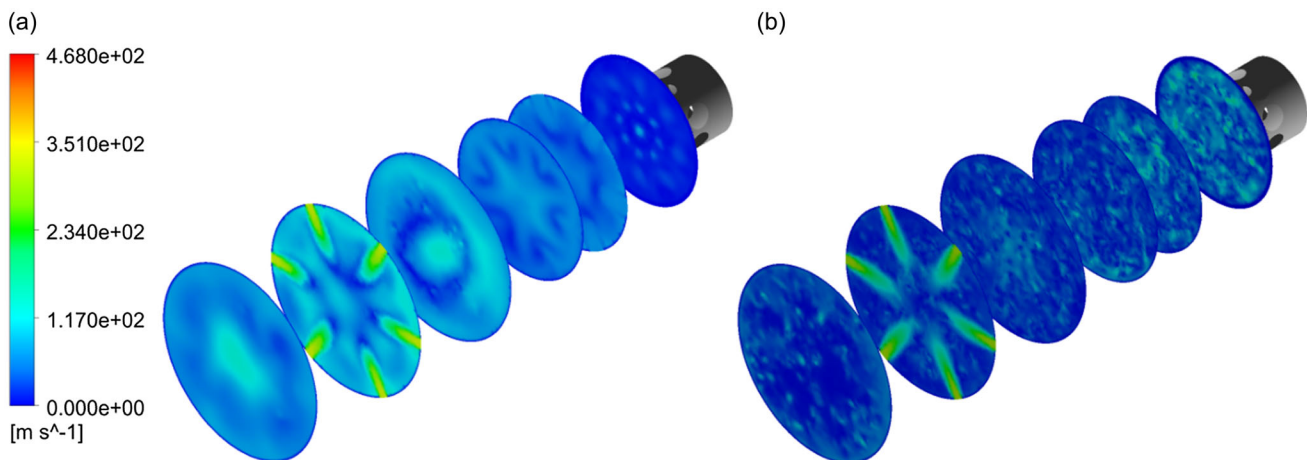


**Figure 9.** Velocity contours inside the chamber: a) stationary state and b) 12 kPa transient case.

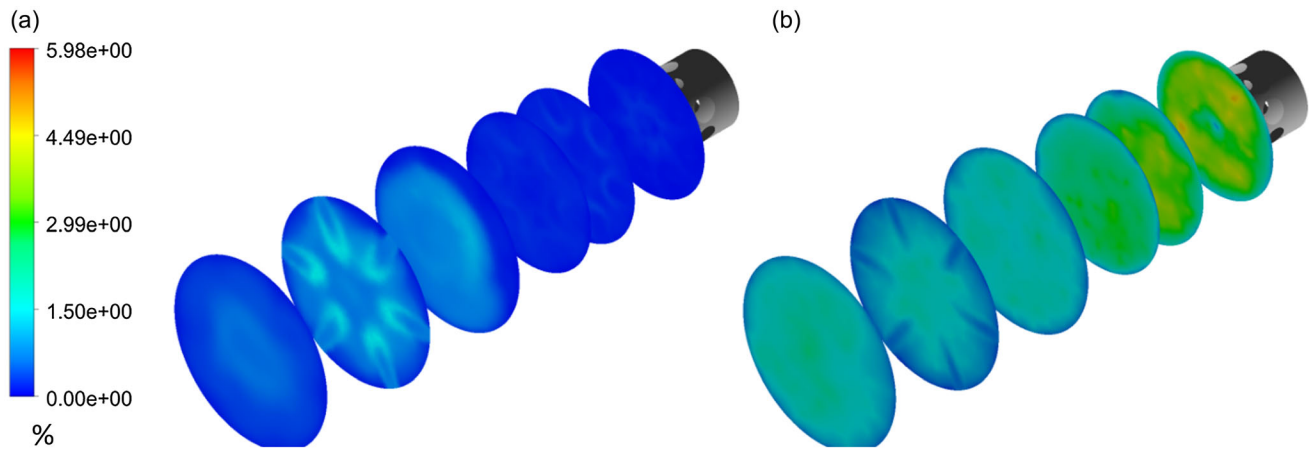


**Figure 10.** Turbulence intensity inside the chamber: a) stationary state and b) 12 kPa transient case.

## 5. Conclusions

Combustion instabilities play a main role in combustion chambers performance including flow dynamics and emissions. This article presented results for 3D computational modelling of combustion in can combustor gas turbine, conducted with time dependence simulations. The study considered a NPCM using natural gas as fuel. Pressure perturbations of 6, 9, and 12 kPa applied to inlet air stream allowed to analyze the effects on the combustion process and flow dynamics. The following conclusions were derived: 1) Pressure and temperature fields in combustor fluctuated according to the induced pressure variations. Zones near the burner, primary air inlet, and cross-flame pipes were observed to be more affected. In the 12 kPa case, a drop-down of pressure was detected at burner surroundings leading to hot gases propagation upstream the air inlet, with flame risk in the crossfire pipe region, making it as flash back process with subsequent thermal fatigue. 2) Emissions such as CO, CO<sub>2</sub>, and NO<sub>x</sub> exhaust gases are sensitive to pressure imbalances. Higher CO and lesser CO<sub>2</sub> exhaust emissions were generated by instabilities which also affected combustion efficiency. 3) Exit combustor emissions revealed a similar frequency for CO, CO<sub>2</sub>, but different for NO<sub>x</sub>, compared to pressure perturbation. 4) It was found that the lowest generation of NO<sub>x</sub> took place for the condition of no perturbation of pressure, the steady-state solution. Instead, the exhaust levels NO<sub>x</sub> increased for the maximum perturbation of pressure. 5) At combustor outlet, strong temperature fluctuations were identified due to pressure perturbations. The 12 kPa showed the highest peaks of temperature which are related to thermoacoustic instabilities. 6) Velocity of flow was affected by the pressure oscillations at combustor inlet. As consequence, turbulence increased from dilution zone to primary air inlet zone.

## Acknowledgements

The National Council for Science and Technology granted financing through project CONACYT-102167. O.T-P. thanks to CONACYT for scholar grant 206393.

## Conflict of Interest

The authors declare no conflict of interest.

## Data Availability Statement

The data that support the findings of this study are available from the corresponding author upon reasonable request.

## Keywords

combustion chamber, combustion instabilities, computational fluid dynamics (CFD), non-premixed combustion, pressure unbalance

Received: September 6, 2023

Revised: November 26, 2023

Published online:

- [1] N. Aldi, M. Morini, M. Pinelli, P. R. Spina, A. Suman, M. Venturini, *Energy Procedia* **2014**, *45*, 1057.
- [2] K. S. Lakeh, A. Martinelli, De La Torre, A. G. Montenegro, A. Onorati, *Energy Procedia* **2015**, *82*, 258.
- [3] S. S. Talebi, A. M. Tousi, *Appl. Therm. Eng.* **2017**, *115*, 517.
- [4] M. P. Auer, T. Hirsch, T. Sattelmayer, in *Proc ASME Turbo-Expo Conf. Paper No. GT-2006-90127*, Barcelona **2006**, pp. 97–106, <https://doi.org/10.1115/GT2006-90127>.
- [5] N. Papafillippou, M. A. Chishty, R. Gebart, *Flow, Turbul. Combust.* **2022**, *108*, 461.
- [6] M. D. Turrell, P. J. Stopford, K. J. Syed, E. Buchanan, in *Proc ASME Turbo Expo Conf. GT2004-53112*, Vienna **2004**, pp. 31–38, <https://doi.org/10.1115/GT2004-53112>.
- [7] D. Lee, J. Park, J. Jin, M. Lee, *J. Mech. Sci. Technol.* **2011**, *25*, 1871.
- [8] M. A. Habib, M. Elshafei, M. Dajani, *Comput. Fluids* **2008**, *37*, 12.
- [9] S. J. Shanbhogue, T. C. Lieuwen, in *Proc ASME Turbo Expo Paper GT2006-90302*, Barcelona **2006**, pp. 247–254, <https://doi.org/10.1115/GT2006-90302>.
- [10] Z. M. Ibrahim, F. A. Williams, S. G. Buckley, J. C. Y. Lee, in *Proc ASME Turbo-Expo Conf. Paper No. GT-2006-90096*, Barcelona **2006**, <https://doi.org/10.1115/GT2006-90096>.

- [11] K. Hoerzer, H. Haselbacher, in *Proc ASME paper GT2004-53517*, Vienna **2004**, <https://doi.org/10.1115/GT2004-53517>.
- [12] A. A. A. Gamil, T. Nikolaidis, I. Lelaj, P. Laskaridis, *Case Stud. Therm. Eng.* **2020**, *22*, 100772.
- [13] S. K. Dhanuka, J. E. Temme, J. F. Driscoll, H. C. Mongia, *Proc. Combust. Inst.* **2009**, *32*, 2901.
- [14] A. Toffolo, M. Masi, A. Lazzaretto, *Appl. Therm. Eng.* **2010**, *30*, 544.
- [15] C. H. Sohn, H. C. Cho, *J. Mech. Sci. Technol.* **2005**, *19*, 1811.
- [16] F. Z. Sierra, J. Kubiak, G. Urquiza, in *ASME Paper GT2004-53658*, Vienna **2004**, <https://doi.org/10.1115/GT2004-53658>.
- [17] F. Z. Sierra, J. Kubiak, G. Gonzalez, G. Urquiza, *Appl. Therm. Eng.* **2005**, *25*, 1127.
- [18] Y. Park, M. Choi, K. Kim, X. Li, ChS. JungNaNa, S., G. Choi, *Energy* **2020**, *213*, 118769.
- [19] H. K. Kayadelen, *J. Nat. Gas Sci. Eng.* **2017**, *45*, 456.
- [20] M. Y. Orlov, I. A. Zubrilin, R. A. Zubrilin, *Procedia Eng.* **2017**, *176*, 394.
- [21] D. Zhao, C. Ji, X. Li, S. Li, *Int. J. Heat Mass Transfer* **2015**, *86*, 309.
- [22] T. K. Ibrahim, M. K. Mohammed, W. H. A. A. Doori, A. T. Al-Sammarraie, F. Basrawi, *J. Adv. Res. Fluid Mech. Therm. Sci.* **2019**, *57*, 228.
- [23] P. Puspitasari, A. Andoko, P. Kurniawan, *IOP Conf. Ser.: Mater. Sci. Eng.* **2021**, *1034*, 012156.
- [24] S. G. Goebel, N. Abuaf, J. A. Lovett, C. P. Lee, in *Proc ASME Turbo-Expo Conf. Paper, 93-GT-228, V03AT15A079*, Cincinnati, OH **1993**, <https://doi.org/10.1115/93-GT-228>.
- [25] Fluent Inc., *Fluent V6.2 User's Guide*, Vol. 3, Canterra Resource Park, 10 Cavendish Court, Lebanon, NH **2010**.
- [26] P. J. Roache, *Verification and Validation in Computational Science and Engineering*, Hermosa Publishers, NM **1998**.
- [27] B. E. Launder, D. B. Spalding, *Mathematical Models of Turbulence*, Academic Press, London **1972**.
- [28] F. Z. Sierra-Espinosa, C. J. Bates, T. O'Doherty, *Comput. Fluids* **2000**, *29*, 215.
- [29] *Simulation and Modeling of Turbulent Flows* (Eds: T. B. Gatski, M. Y. Hussaini, J. L. Lumley), Oxford University Press, NY **1996**.
- [30] J. H. Ferziger, M. Peric, *Computational Methods for Fluid Dynamics*, Springer Science & Business Media, Heidelberg **2012**.
- [31] S. Klayborworn, W. Pakdee, *Case Stud. Therm. Eng.* **2019**, *14*, 100451.
- [32] Z. Ren, G. M. Goldin, V. Hiremath, S. B. Pope, *Fuel* **2013**, *105*, 636.
- [33] S. Benaissa, B. Adouane, V. Ali, S. S. Rashwan, Z. Auachria, *Therm. Sci. Eng. Prog.* **2022**, *27*, 101178, ISSN 2451-9049.
- [34] G. Smith, M. Golden, M. Frenklach, N. Moriarty, B. Eiteneer, M. Goldenberg, C. Bowman, R. Hanson, S. Song, W. Gardiner, Jr, V. V. Lissianski, *Gri 3.0 Mechanism*, Gas Research Institute, Des Plaines, IL **1999**.
- [35] R. Viskanta, *Radiative Transfer in Combustion Systems: Fundamentals and Applications*, Purdue University, IN **2005**.
- [36] Y. Zeldovich, P. Y. Sadvnikov, D. A. Frank-Kamenetskik, *Oxidation of Nitrogen in Combustion*, Academy of Science of SR, Institute of Chemical Physics, Moscow, Leningrad **1947**.
- [37] O. Tenango-Pirin, *Doctorate Thesis*, Universidad Autónoma del Estado de Morelos (Cuernavaca, México) **2017**.
- [38] S. E. Kim, X. Zhu, S. Orsino, in *Proc. ASME 2005 Fluids Engineering Division Summer Meeting*, Houston TX **2005**, pp. 307–316, <https://doi.org/10.1115/FEDSM2005-77085>.
- [39] F. Z. Sierra, D. Narzary, C. Bolaina, J. C. Han, J. Kubiak, J. S. Nebradt, *Proc. Turbo Expo: Power Land, Sea, Air* **2009**, *48845*, 115.
- [40] I. Ieronymidis, R. H. Gillespie, P. T. Ireland, in *Proc. Turbo Expo: Power for Land, Sea, and Air. ASME Paper GT2006-91231*, Barcelona **2006**, <https://doi.org/10.1115/1.3140283>.
- [41] G. V. Kuznetsov, M. A. Sherement, *Int. J. Heat Mass Transfer* **2009**, *52*, 2215.
- [42] R. Marsh, J. Runyon, A. Giles, S. Morris, D. Pugh, A. Valera-Medina, P. Bowen, *Proc. Comb. Inst.* **2017**, *36*, 3949.